

An assessment of the Ring of Fire approach for indoor and outdoor on-site sports aerodynamic investigation

Spoelstra, Alexander; de Martino Norante, Luigi; Terra, Wouter; Sciacchitano, Andrea; Scarano, Fulvio

Publication date

2018

Document Version

Final published version

Published in

Proceedings of the 19th international symposium on application of laser and imaging techniques to fluid mechanics

Citation (APA)

Spoelstra, A., de Martino Norante, L., Terra, W., Sciacchitano, A., & Scarano, F. (2018). An assessment of the Ring of Fire approach for indoor and outdoor on-site sports aerodynamic investigation. In *Proceedings of the 19th international symposium on application of laser and imaging techniques to fluid mechanics*

Important note

To cite this publication, please use the final published version (if applicable).
Please check the document version above.

Copyright

Other than for strictly personal use, it is not permitted to download, forward or distribute the text or part of it, without the consent of the author(s) and/or copyright holder(s), unless the work is under an open content license such as Creative Commons.

Takedown policy

Please contact us and provide details if you believe this document breaches copyrights.
We will remove access to the work immediately and investigate your claim.

An assessment of the Ring of Fire approach for indoor and outdoor on-site sports aerodynamic investigation

Alexander Spoelstra^{1*}, Luigi de Martino Norante¹, Wouter Terra¹, Andrea Sciacchitano¹ and Fulvio Scarano¹

¹: Aerospace Engineering Department, Delft University of Technology, Kluyverweg 2, Delft, 2629 HT, The Netherlands

* Correspondent author: A.M.C.M.G.Spoelstra@tudelft.nl

Keywords: Large-scale PIV, HFSB, on-site, sports aerodynamics

ABSTRACT

The Ring of Fire measurement system is deployed for the measurement of the aerodynamic drag of transiting cyclists. The drag force is evaluated using large-scale stereoscopic PIV and invoking the conservation of momentum within a control volume in a frame of reference moving with the athlete. Two experiments are carried out that yield the cyclist aerodynamic drag in time-trial and upright position in indoor and outdoor conditions. The rider cycles at a velocity of approximately 5 m/s and 8 m/s for respectively the indoor and outdoor experiment, corresponding to a torso based Reynolds number of 2.1×10^6 and 3.2×10^6 . The indoor measurements are conducted at a rate of 8 Hz within a measurement plane of approximately 1.8×2.4 m. The outdoor measurements are conducted at a rate of 2000 Hz within a measurement plane of approximately 1.8×1.8 m. Neutrally buoyant helium-filled soap bubbles are used as flow tracers. Despite the fact that two different cyclists and two different bikes were used and that the local angle of attack of the body was different, the streamwise velocity and vorticity fields compare well between both experiments and to literature. Results from both experiments show the same peak momentum deficit as well as the same main and secondary vortices. A clear distinction in upright vs. time-trial ensemble-averaged drag area is found for both experiments. Furthermore, the indoor experiment shows it is possible to distinguish smaller variations in the drag area between two postures, namely between a time-trial asymmetric and symmetric configuration. Small drag differences ($\approx 5\%$) with less than twenty samples per case are detected.

1. Introduction

In elite cycling the role of aerodynamics is crucial in that a reduction of the aerodynamic drag has direct consequences on the athlete's race time (Kyle and Burke 1984, Wilson 2004, Lukes et al. 2005). Several approaches for investigation of cycling aerodynamics have been proposed in the past, including wind tunnel measurements, track testing and numerical simulations by Computational Fluid Dynamics (CFD). Wind tunnel measurements are typically carried out by force balance to quantify the aerodynamic loads acting on the cyclist. The tests typically involve variations of the cyclist's posture and equipment to determine the configuration that yields the minimum aerodynamic drag (Gibertini and Grassi 2008, among others). Balance measurements in wind tunnels allow for accurate conditioning of the flow environment and a high repeatability; however, they may be qualified as 'blind' as they give no information about the

flow field and the specific sources of drag. Recently, several studies have made use of different techniques to achieve a quantitative visualization of the flow field around a cyclist model. Crouch et al. (2014) conducted an extensive investigation of the aerodynamics of a pedalling cyclist model using dynamic pressure measurements by four-hole probe, force measurements by six-component balance, surface pressure measurements and oil flow visualization. The authors observed a complex system of streamwise vortices in the wake of the cyclist, which varied with the legs position along the crank cycle. Furthermore, they concluded that variations of the aerodynamic drag throughout a crank cycle cannot be ascribed only to the change in frontal area, but are better explained through the effect that the legs position has on the large-scale flow structures in the cyclist's wake. More recently, large-scale Particle Image Velocimetry (PIV) measurements have been conducted at Delft University of Technology on a full-scale, static replica of the 2017 Giro d'Italia winner Tom Dumoulin (Terra et al. 2016, Shah 2017). The flow measurements in the wake of the cyclist model confirmed the presence of a system of counter-rotating vortex pairs emanating from feet, the knee of the stretched leg, the hips and the thighs. It was noticed that, when the legs position is asymmetrical with one leg stretched and one bent upwards, also the cyclist's wake is asymmetrical and exhibits higher momentum deficit on the side of the stretched leg. For the asymmetric leg position a more complete insight on the three-dimensional flow structure around the cyclist and in his near wake was achieved by Jux et al. (2018) by means of robotic PIV measurements.

As an alternative approach to wind tunnel measurements, aerodynamic data can be retrieved from in-field track measurements where the athlete is in motion and real racing conditions can be simulated (e.g. no bike supports, no static model, no need of rolling floor). Track measurements typically rely upon quantification of the mechanical power output of the athlete at a constant velocity (Gibertini et al., 2010) or upon the deceleration of the non-pedalling cyclist (Candau et al., 1999). A balance between the mechanical power delivered by the athlete and the power dissipated by air resistance and rolling resistance between tires and floor yields the aerodynamic drag. However, the uncertainty of the coefficient of rolling resistance makes this approach more suitable to estimate aerodynamic drag variations among different configurations, rather than the absolute aerodynamic drag value in a specific configuration. Furthermore, also this approach is regarded as blind because it does not provide information on the local sources of aerodynamic drag.

Contrary to most measurements in wind tunnels and on-track, results obtained from computational fluid dynamics simulations provide information on both the flow field and the drag force. Most of these simulations are conducted via (U)RANS or unsteady LES (Defraeye et al. 2010, Blocken et al. 2013, Griffith et al. 2014, among others). However, due to the complexity of the three-dimensional unsteady flow around a cyclist, those simulations often suffer of low accuracy and require validation experiments. Steady models are typically employed, which give limited information on the actual aerodynamics occurring during competitions, when the athlete is in motion.

From the above discussion, it emerges that none of the techniques typically employed for cycling aerodynamics is able to provide an accurate drag estimate of a cyclist in race conditions as well as visualize the corresponding flow field. In this work, we propose a novel measurement approach, the Ring of Fire, which aims at yielding accurate drag measurement and quantitative flow visualizations during a cyclist's training on a track. The flow measurements are conducted by large-scale PIV and the aerodynamic drag is estimated via the application of conservation of momentum in a control volume enclosing the model (e.g. Kurtulus et al., 2007).

The present work demonstrates the feasibility of the Ring of Fire on a full-scale cyclist in different conditions. Two experiments are presented, an indoor experiment and an outdoor experiment. Both experiments make use of Helium filled soap bubbles (HFSB) as flow tracers, because of their high light scattering efficiency and tracing fidelity (Bosbach et al., 2009, and Scarano et al., 2015, among others). The results discuss multiple cyclist postures (time trial, upright, static legs and dynamic legs) in terms of flow visualizations and drag measurements, both instantaneous as well as ensemble-averaged.

2. Working principle

To explain the working principle of the ring of fire approach, let us consider a cyclist riding a bike and therefore moving at velocity u_c with respect to a fixed frame of reference. For simplicity, the cyclist's velocity u_c is assumed constant. Let us take a control surface normal to the direction of motion of the cyclist. Prior to the passage of the cyclist, the air in the control surface features a certain velocity u_{env} , which in general is non-null, non-uniform and non-stationary, as depicted in Fig. 1-top. After the passage of the cyclist, a wake velocity u_{wake} develops from the interaction between the moving cyclist and the surrounding air. It is assumed

that the in-plane gradient of the environmental fluctuations is negligible with respect to the ones in the wake. If we now consider a frame of reference moving with the cyclist at speed u_c , the air flow velocity far in front of the cyclist is $U_\infty = u_{env} - u_c$, whereas the flow velocity in the back of the cyclist is $U = u_{wake} - u_c$ (Fig. 1-bottom).

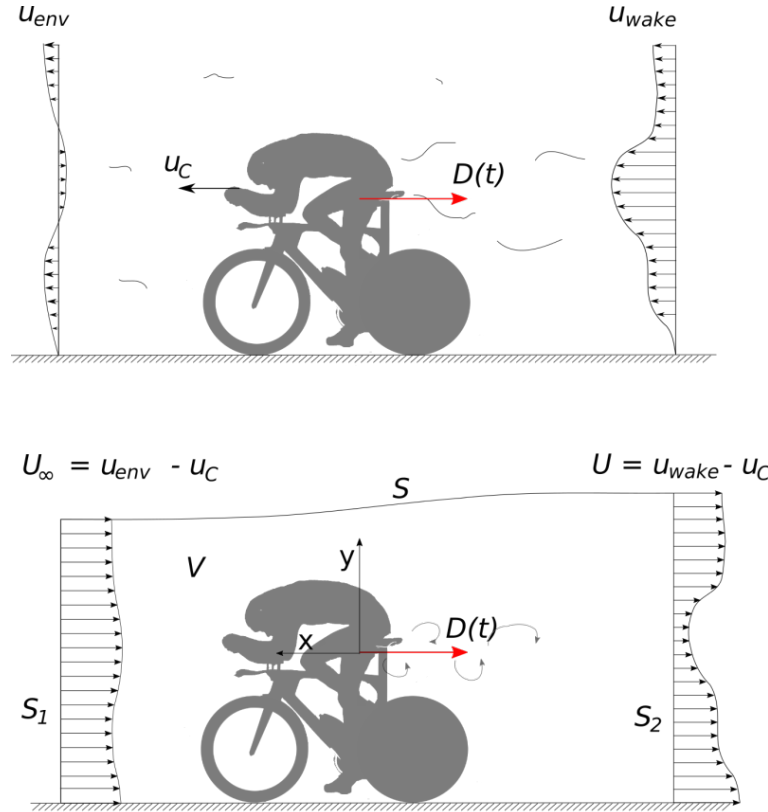


Fig. 1 Schematic view of the aerodynamic drag as a result of the fluid velocity relative to the cyclist in a fixed frame of reference (top) and the frame of reference of the model (bottom).

The aerodynamic drag acting on the cyclist can be expressed using a control volume approach invoking the conservation of momentum in a frame of reference moving with the model (De Kat and Bleischwitz, 2016) assuming stationary upstream conditions. Considering two control surfaces S_1 and S_2 sufficiently far away (upstream and downstream, respectively) from the model, the drag force can be expressed as the difference in momentum flows upstream and downstream of the model (M_1 and M_2 , respectively):

$$D(t) = \underbrace{\rho \iint_{S_1} U_\infty^2 dS}_{M_1} - \underbrace{\rho \iint_{S_2} U^2 dS}_{M_2} \quad (1)$$

where ρ is the fluid density. Equation 1 is rewritten by enforcing mass conservation across the upstream boundary S_1 and downstream boundary S_2 (Anderson, 2016):

$$D(t) = \rho \iint_{S_2} (U_\infty - U) U dS \quad (2)$$

This expression allows to obtain the aerodynamic drag from the surface integral over the wake plane only. Equation 2 holds in a frame of reference moving with the model. When, instead, the velocity is measured in a fixed frame of reference (lab frame of reference), the aerodynamic drag is expressed as:

$$D(t) = \rho \iint_{S_2} (u_{wake} - u_{env})(u_c - u_{wake}) dS \quad (3)$$

where u_c is the velocity of the cyclist. The time-average drag of the cyclist during one passage is determined from the time-average of Equation 3. Finally, a statistical analysis considering multiple passages of the cyclist yields the ensemble-averaged drag and its uncertainty.

3. Experimental setup and procedure

3.1 Measurement system and conditions

The experimental conditions and the corresponding tested object and facilities are presented in Tab. 1. Both the experiments are performed in an in-house built duct, which has the primary objective of maintaining a sufficient seeding density within the measurement area to enable stereoscopic-PIV image analysis. Curtains are used to close both the entrance and the exit in the outdoor experiment and only the exit in the indoor experiment. Near the half length of the duct, a laser cut-out is realized to provide optical access for the laser light. The floor of the tunnel is covered with a carpet (Polypropylene, 3 mm) used to avoid ground slippery conditions due to the PIV seeding. A picture of the setup of the two experiments is shown in Fig. 2 and Fig. 3. During the indoor experiment the cameras were positioned 6 m in upstream of entrance of the tunnel and, hence, are not visible in Fig. 2.

The tested object corresponds to two different amateur cyclists with approximate torso length of $D = 600$ mm, equipped with a time-trial skin-suit and helmet and riding a time-trial bike: in the indoor experiment the bike is a Team Sunweb time-trial bike with a Giant Trinity TT Advanced Pro frame, while a Ridley Cheetah frame is used in the outdoor experiment. Although the two experiments have similar acceleration length before the laser plane, the cyclist has strong space limitations for braking in the indoor experiment: this is the origin of a difference in the cyclist velocity, yielding a torso-based Reynolds number equal to 2.1×10^5 in the indoor experiment and 3.2×10^5 in the outdoor one.

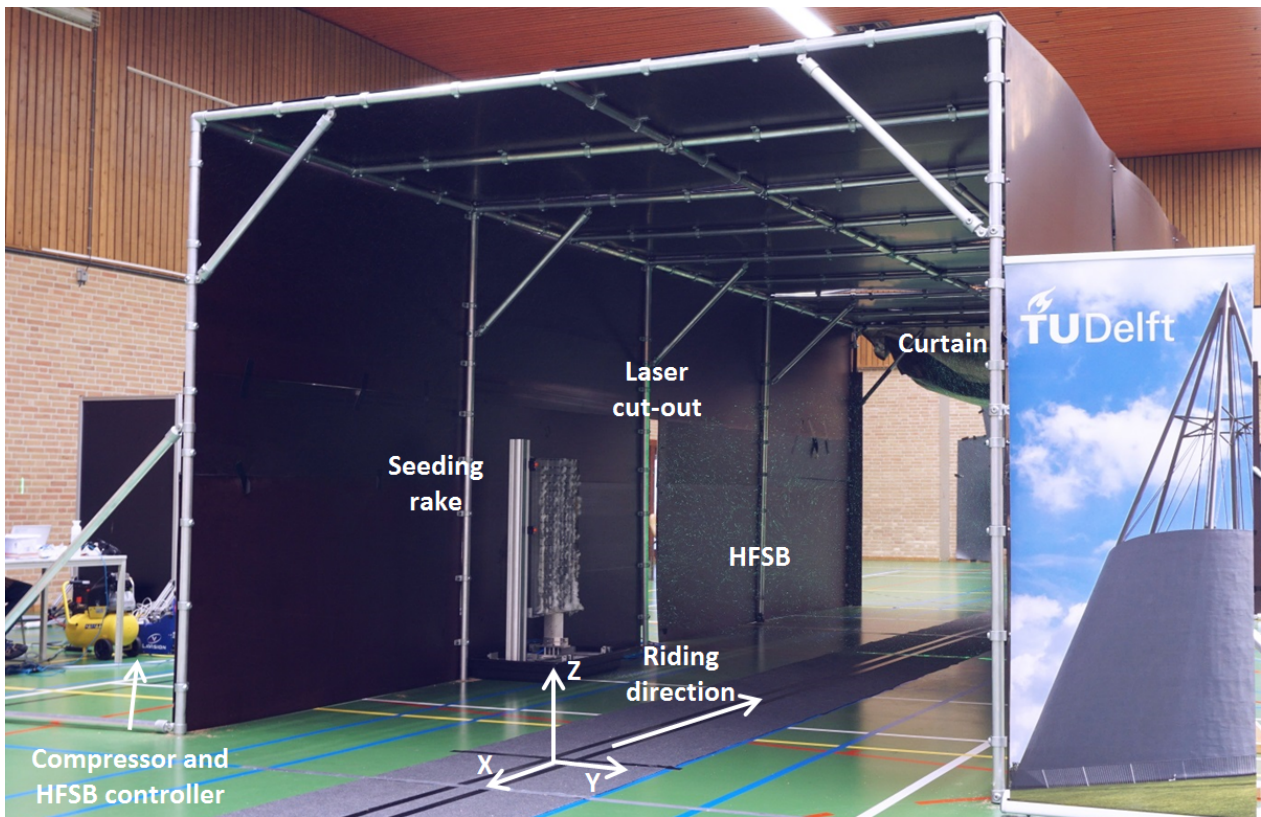


Fig. 2 View of the indoor experimental setup.

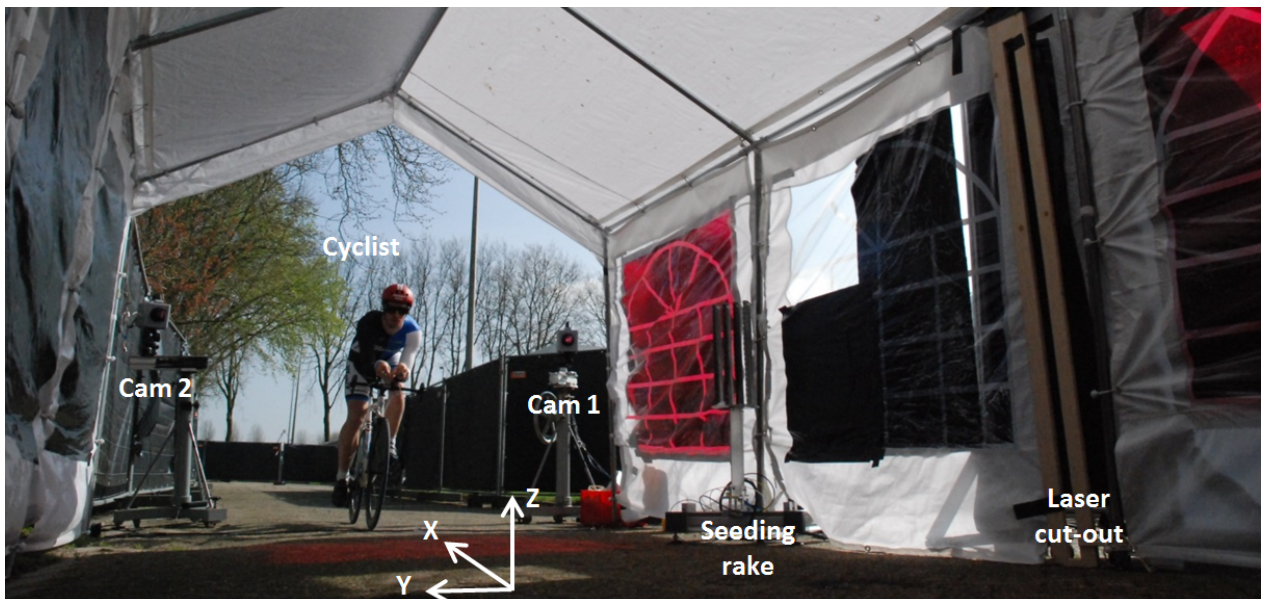


Fig. 3 View of the outdoor experimental setup.

In both the cases, measurements are conducted with the cyclist in upright and time-trial position (see Fig. 4), but with a substantial difference in the reduced frequency $k = \frac{2r\pi f}{u_c}$, where r is the

bike crank length, f the cadence and u_c the cyclist velocity, as reported in Tab. 1. In the indoor experiment, in addition to the conventional pedalling conditions, two static conditions (fixed legs position) are tested in time-trial configuration: the cyclist stops pedalling 12 m before the laser plane by keeping a constant crank angle φ equal to 75° and 15° , respectively. The former corresponds to an asymmetric condition with the right leg extended, while the latter to a symmetric condition with the thighs aligned with respect to each other.

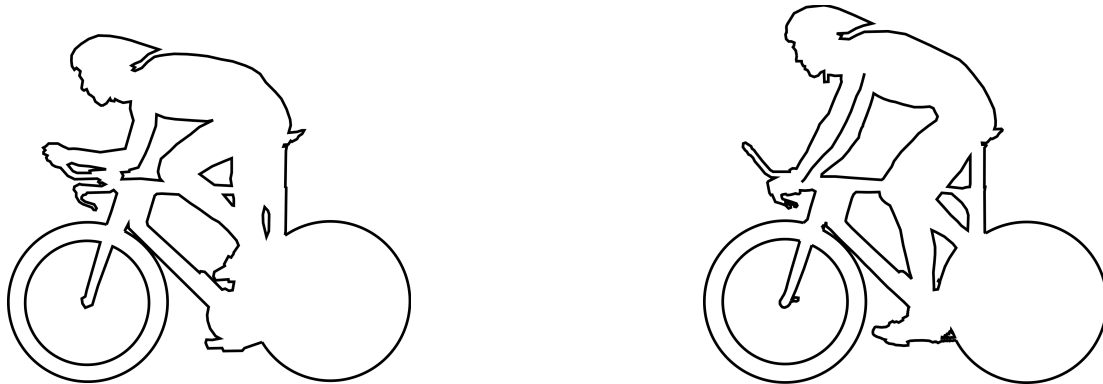


Fig. 4 Tested cyclist postures in the two experiments, silhouette reproduced from the cyclist of the indoor experiment. **Left:** time-trial posture. **Right:** (brake hoods) upright posture.

The crank angle value is based on the convention illustrated in Fig. 5: the angle φ is related to the angular position of the right foot with respect to the zero angle, defined as the position at which the crank is horizontal and with the right foot forward. The crank angle is positive for crank rotations in the sense of pedalling forward.



Fig. 5 Bike crank angle convention.

Tab. 1 Overview of the measurement conditions of the two experiments

	Indoor	Outdoor
Duct dimensions [m ³]	10×4×3 [x,y,z]	6×3×2 [x,y,z]
Solid blockage [%]	3.5	7
Cyclist velocity (u_c) [m/s]	5.3 ± 0.1	8.3 ± 0.2
Reduced pedalling frequency (k)	0.12	0.23
Crank length [mm]	175	172.5
Zero degree crank	Horizontal, right front	Horizontal, right front
Gear ratio	53/12	42/18
Acceleration length [m]	31	30
Deceleration length [m]	15	40
Torso based Reynolds number	2.1×10^5	3.2×10^5

3.2 PIV hardware and imaging

Both the experiments are performed with a Large-scale PIV system and their respective setup parameters are presented in Tab. 2. Neutrally buoyant Helium Filled Soap Bubbles (HFSB) are used with an average diameter between 0.3 and 0.4 mm, providing sufficient light scattering to visualise a field of view (FOV) of the order of 3 m². The tracers are injected into the duct by a 200 nozzles rake in the indoor experiment and a 80 nozzles one in the outdoor experiment, after which they spread within the duct. A LaVision GmbH HFSB generator controls pressurised air and helium rates towards the seeding rake while fed by a 200L helium vessel and compressed air, which is provided by a Stanley® DL/250/10/24 compressor in the indoor experiment.

While using the same flow tracers, the two experiments make use of different Stereo-PIV setup. In the indoor one, a low-speed PIV system is used, consisting of a Quantel Evergreen 200 Nd:YAG FL laser and two CCD Imperx Bobcat IFV-B1610 cameras (see Tab. 2 for specifications). In the outdoor experiment, a high-speed system is used, featuring a Quantronix Darwin Duo Nd:YLF laser and two CMOS Photron FastCAM SA1 cameras. On one hand the low-speed system benefits of light energy one order of magnitude higher than the high speed system, and pixel size one order of magnitude smaller. This explains the necessity of larger object-cameras distance to visualise similar FOV dimensions and the possibility to increase the laser sheet thickness as well. On the other hand, the high-speed system benefits of an acquisition frequency

three orders of magnitude higher than the low-speed system (2000Hz vs. 8Hz), allowing time-resolved measurements of the cyclist's wake. With the low-speed system, classical Double-Pulse Double-Frame PIV is employed, with the pulse separation constrained by the out-of-plane loss-of-correlation factor (Keane and Adrian, 1992). From the above described equipment and conditions, the setup parameters were determined and can be compared in Tab. 2.

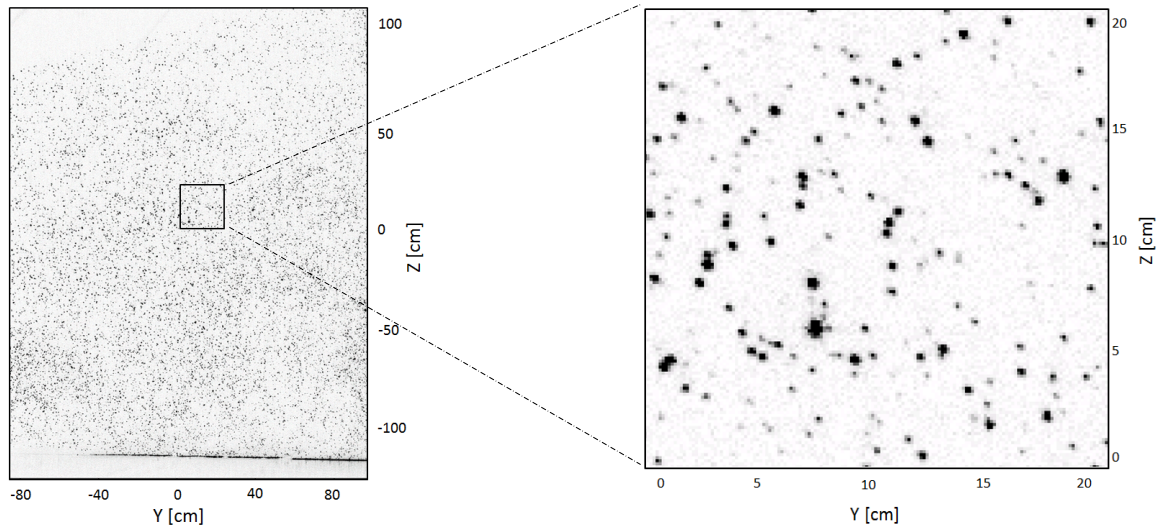
Tab. 2 Equipment and setup parameters

		Equipment	
Purpose	Instrument	Indoor (Low-speed PIV)	Outdoor (High-Speed PIV)
Imaging	Cameras	Imperx Bobcat IGV-B1610 cameras (CCD, 1628 × 1236 pixels, pixel pitch of 4.4 μm, 14 bits)	Photron FastCAM SA1 cameras (CMOS, 1024 × 1024 pixels, pixel pitch of 20 μm, 12 bits)
	Objectives	2 × AF Nikon $f = 35mm$	2 × Nikon $f = 50mm$
	Others	Bandpass filters	Bandpass filters
Illumination	Laser	Quantel Evergreen 200 Nd:YAG FL laser (2 × 200 mJ at 15 Hz)	Quantronix Darwin Duo Nd:YLF laser (2 × 25 mJ at 1 kHz)
Seeding	Tracer particles Seeding rake	Helium-Filled Soap Bubbles 200 nozzles divided over 10 vertical wings	Helium-Filled Soap Bubbles 80 nozzles divided over 4 vertical wings
Data Collection	Software	Davis – Lavision, v8.1.2	Davis – Lavision, v8.3.1
		Setup parameters	
Purpose	Parameter	Indoor (Low-speed PIV)	Outdoor (High-Speed PIV)
Field of View	X (thickness) [m]	0.04	0.03
	Y (Width) [m]	1.8	1.8
	Z (Height) [m]	2.4	1.8
Imaging	$f_{\#}$	5.6	5.6
	Magnification	0.00297	0.0111
	Object distance [m]	11.5	4
	Digital image Resolution [mm/px]	1.5 mm/px	1.8 mm/px
	Total view angle cameras [°]	28	31
Acquisition	f_{acq} [Hz]	8	2000
Pulse separation	Δt [ms]	3	0.5
Seeding Concentration	particle imaging density	0.11 particles/pixel	0.09 particles/pixel

The accuracy of the PIV measurement is highly dependent on the quality of the image recordings. A typical recording for both experiments is shown in Fig. 6. Comparing the left images of both, it is observed that the particles are distributed more uniformly over the FOV of the indoor experiment, which in turn leads to less erroneous vectors. Furthermore, the particle

image diameter (2px vs. 0.5px) as well as the image signal-to-noise ratio SNR (20 vs. 10) are larger for the indoor experiment. It can be concluded that the overall image quality of the indoor experiment is higher and thus a more precise velocity estimation is expected from the latter.

Indoor



Outdoor

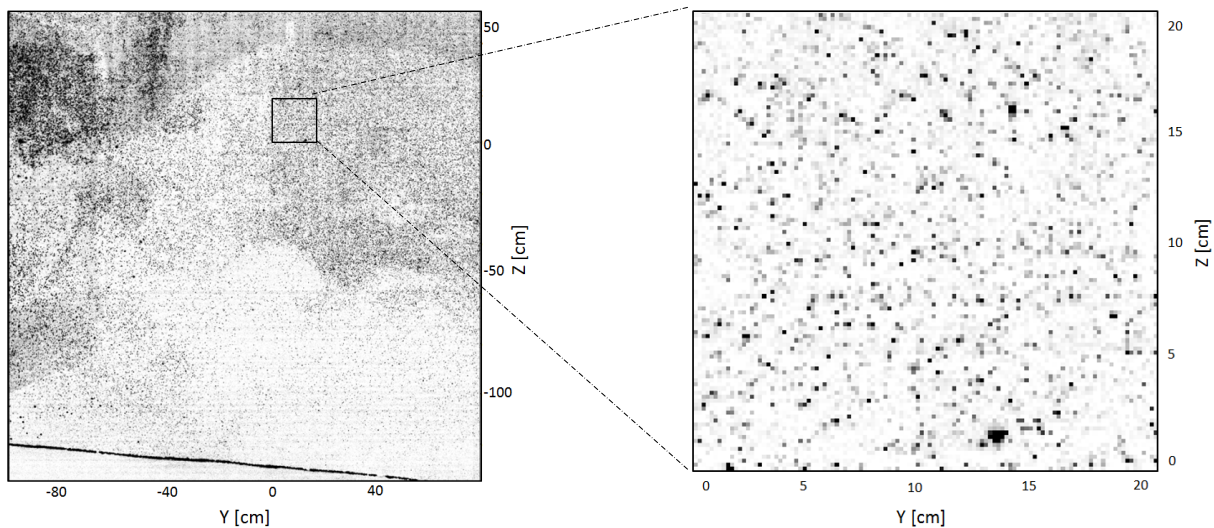


Fig. 6 Top: indoor experiment. **Bottom:** outdoor experiment. **Left:** Raw image from camera 1 (intensity with inverted colours). **Right:** Detail of the particle images.

3.3 Data processing

The collected images are processed through a Stereoscopic correlation algorithm, after pre-processing of the images aiming at improving image SNR. While in the indoor experiment the standard cross-correlation is used, a sliding sum of correlation algorithm (Sciacchitano et al.,

2012) is necessary in the outdoor experiment, due to lack of uniform seeding distribution and consequent empty spots in the field of view. A summary of the processing parameters and PIV performances is shown in **Error! Not a valid bookmark self-reference..**

The instantaneous drag force for each model passage is computed via equation 3 considering the flow momentum deficit between downstream and an upstream plane with respect to the cyclist. In both experiments, u_{env} is evaluated by averaging the velocity field prior to the passage of the cyclist over time.

Evaluation of the aerodynamic drag through equation 3 requires information of the cyclist's speed. In the outdoor experiment, one of the high-speed cameras is used to obtain the cyclist's speed at the measurement plane, by measuring the time it takes for the entire bike to cross the measurement plane. For each passage, the cyclist's speed is assumed constant and used to evaluate the drag for each wake locations. Instead, in the indoor experiment the bike was equipped with a magnetic sensor providing cyclist speed information to a bike computer: this allows to know the full position and velocity history of the cyclist and minimise the error introduced by the assumption of a streamwise constant speed.

Ensemble-averaged velocity fields are obtained for each of the tested configurations from ten cyclist passages for the outdoor experiment, twenty for the indoor static tests and thirty for the indoor dynamic ones. The Ring of Fire experiments suffer from two main repeatability issues that require manipulation of the instantaneous data to retrieve ensemble-averaged flow fields. As the cyclist crosses the measurement plane at a different y coordinate for every passage, each instantaneous measurement is mapped onto a common grid to relocate the time-average wake flow structure with respect to the cyclist. Moreover, because of a lack of synchronisation between the image acquisition and the cyclist passage, each instantaneous test presents a slightly different streamwise relative position of the cyclist with respect to the wake planes. In both the experiments a manual streamwise relocation procedure has been applied, with the High-speed PIV system providing a better streamwise resolution of the cyclist's streamwise position due to the system higher acquisition frequency.

Tab. 3 Data processing

Parameter	Indoor	Outdoor
Correlation Algorithm	Classical cross-correlation	Sliding sum-of-correlation algorithm
Interrogation windows	64 x 64 pixels (95 x 95 mm ²)	64 x 64 pixels (116 x 116 mm ²)
Overlap factor	75%	75%
Vector pitch	24 mm	29 mm

Dynamic Spatial Range	25	15
Dynamic Velocity Range	250	100

3.4 Measurement Procedure

Before the passage of the athlete, the duct curtains are closed to enable accumulation of the HFSSBs seeding for about two minutes. Atmospheric conditions require continuous operation of the seeding generator for the outdoor experiment. Instead, in the indoor experiment the bubbles production is interrupted prior to the passage of the cyclist, to minimize the influence of the momentum introduced by the seeding rake.

The cyclist starts from rest always at the same crank angle and from the same streamwise position for each passage. The crank angle can be directly retrieved from the streamwise location of the cyclist, thus allowing phase-locked averaging of the wake flow fields. However, given the different reduced frequencies, this relation is not identical between the two experiments.

In the indoor experiment, a through-beamer photoelectric sensor triggers the image acquisition with the aim of reducing the synchronisation error, while the user manually triggers the image acquisition in the outdoor experiment. Image acquisition is performed over a range of 22 m in the outdoor tests and 27 m in the indoor ones. While a time-frame between 5 to 10 minutes is necessary for storing the acquired images with the high-speed PIV system, the limited amount of images (typically 20) recorded by the low-speed PIV system permits multiple consecutive passages separated by only one minute. In this case, the experiment time is only bottlenecked by the time required for operating and stopping again the seeding generator.

4. Results

4.1 Quantitative flow visualization

4.1.1. Flow visualization before passage

The undisturbed flow before the passage of the cyclist features a velocity u_{env} , which in general is non-zero, non-uniform and non-stationary due to, among others, environmental conditions (outdoor), seeding injection and climate control (indoor). The flow field before the cyclist's passage is illustrated in Fig. 7 for an individual measurement both of the indoor (left) and outdoor (right) experiment. In order to reduce noise, an average over multiple undisturbed velocity fields before passage is taken. The contour of the out-of-plane (streamwise) velocity component is shown, along with the in-plane (Y-Z) velocity vectors.

The indoor experiment was performed in a closed, controlled environment, whereas during the outdoor experiment moderate wind was present and only partly attenuated by the walls of the duct. This is clearly visible in Fig. 7, where the environment velocity is of the order of a few centimetres per second, whereas it is about four times higher in the outdoor experiment (see also Tab. 4). When the environmental velocity is non-uniform and non-zero, it should be taken into account for in the drag computation via equation 3 as it contributes to the overall momentum. Furthermore, non-stationary conditions will affect the variations in the measured drag, as velocity fluctuations are expected between S_1 and S_2 (Fig. 1).

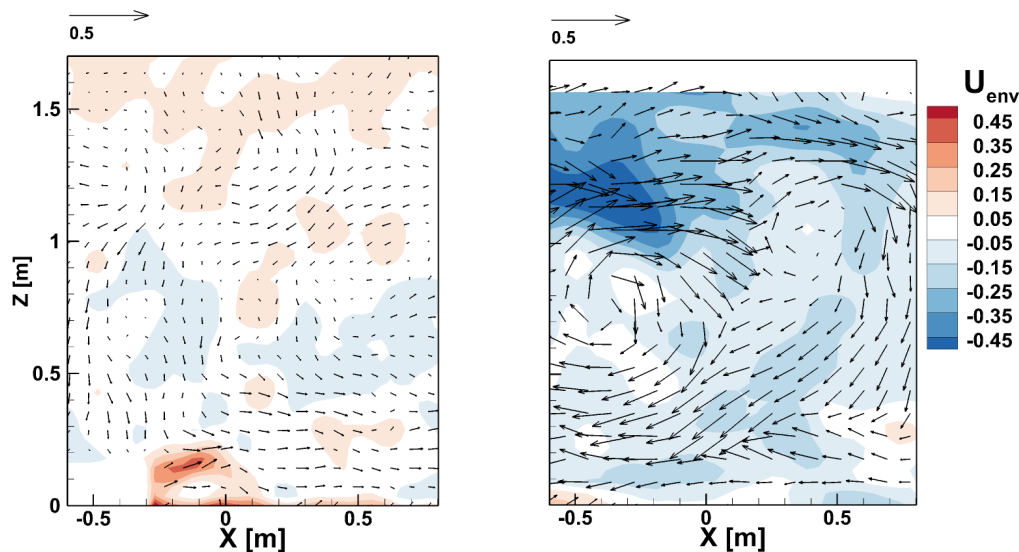


Fig. 7 Velocity field in m/s from one individual measurement before passage of the cyclist. **Left:** Indoor experiment, 3.5 m (0.7 sec) in front of the cyclist; **Right:** Outdoor experiment, 2 m (0.25 sec) in front of the cyclist.

Tab. 4 Ensemble-averaged spatial root-mean-square (rms) of the velocity components of the environmental flow field for both indoor and outdoor experiment.

	$(u_{env})_{rms}$ [m/s]	$(v_{env})_{rms}$ [m/s]	$(w_{env})_{rms}$ [m/s]
Indoor	0.069	0.046	0.026
Outdoor	0.163	0.128	0.079

4.1.2 Flow visualization after passage

The flow fields in the wake of the cyclist are only discussed for the dynamic time-trial configuration and are presented in the coordinate system as shown in Fig. 2 and Fig. 3 with the origin positioned at the rearmost point of the saddle. In order to make the comparison between results from both experiments possible, the flow field variables and time are made dimensionless in the following way:

$$\text{Dimensionless streamwise velocity deficit } u_x: \quad u_x = \frac{u_{wake} - u_{env} + u_C}{u_C} \quad (4)$$

$$\text{Dimensionless streamwise vorticity } \omega_x^*: \quad \omega_x^* = \frac{\omega_x \times D}{u_C} \quad (5)$$

$$\text{Dimensionless time } t^*: \quad t^* = \frac{t \times u_C}{D} \quad (6)$$

Furthermore, the plotted cyclist contours in the figures below do not represent the actual leg position of the athlete, they only give the reader an idea of the size and location of the cyclist with respect to the measurement area.

Fig. 8 shows a comparison of the instantaneous flow fields of the dimensionless streamwise velocity deficit u_x at $t^* = 3$. Both are comparable in terms of out-of-plane velocity distribution and wake shape. A main difference that is observed is the larger wake width in the outdoor Ring of Fire. Two explanations can be thought of: the difference in reduced pedalling frequency ($k_{outdoor} = 0.23$ versus $k_{indoor} = 0.12$), causing larger wake mixing because of higher wake unsteadiness, and the larger environmental fluctuations for the outdoor Ring of Fire. In both the cases the environmental fluctuations have been averaged over a set of upstream planes and subtracted from the specific downstream plane, based on how u_x has been defined in equation 4. This correction for the environmental flow field is more efficient for the indoor Ring of Fire since, within the few seconds between the acquisition of the upstream plane and the wake plane, the outdoor conditions have changed significantly more than is the case for the indoor experiment.

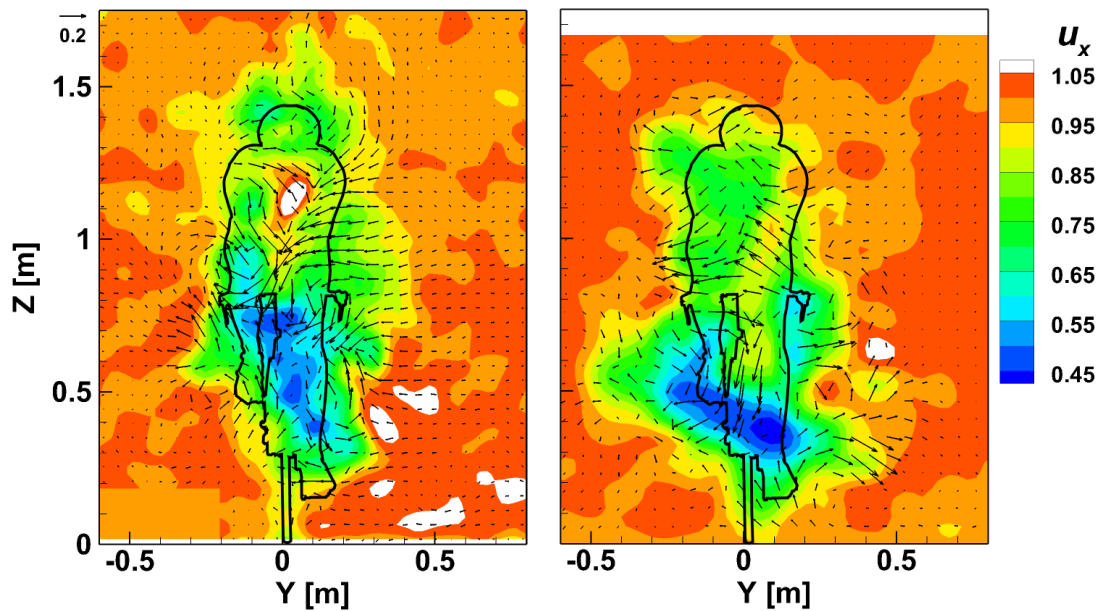


Fig. 8 Dimensionless instantaneous streamwise velocity deficit u_x at $t^* = 3$. **Left:** Indoor experiment ($\varphi = 65^\circ$); **Right:** Outdoor experiment ($\varphi = 320^\circ$).

In Fig. 9, six ensemble-averaged wake planes downstream of the cyclist in dynamic time-trial position, with the same field of view as in Fig. 8, are shown for both the indoor (Fig. 9 - top) and outdoor (Fig. 9 - bottom) Ring of Fire. The ensemble-averaged flow fields are obtained from 20 and 10 individual runs from respectively the indoor and outdoor experiment. The averaging process led to a loss in the field of view in Y-direction caused by the different location of the cyclist for every run. In the near wake of the cyclist, the separated flow exhibits a momentum deficit up to 55% of the freestream velocity. The major loss of velocity corresponds to the wake behind the legs. Along the streamwise direction the wake evolves under a diffusion process: flow entrainment smoothens out the planar gradient of streamwise velocity, so that the wake contour covers a larger area but the lowest velocity value increases. At a certain point this diffusion broadens the wake so much that it is not fully captured anymore within the field of view, which leads to wrongly measured drag values.

The extent of the body separated flow is strongly characterised by couples of counter-rotating structures. In Fig. 10 these wake structures are compared between the different experiments. Positive vorticity relates to counter-clockwise rotating vortices, while negative vorticity to clockwise ones. Despite the fact that two different cyclists and two different bikes were used and that the local angle of attack of the body was different, the vorticity field shows the same main and secondary vortices in both cases, which are also in good agreement to those found in Crouch et al. (2014, 2016). Apart from the head structures, hip, thigh and ankle-calf vortices are present in similar position and with similar relative strength. The stronger vorticity of the head vortices

in the indoor Ring of Fire may be due to a different torso inclination with respect to the free stream.

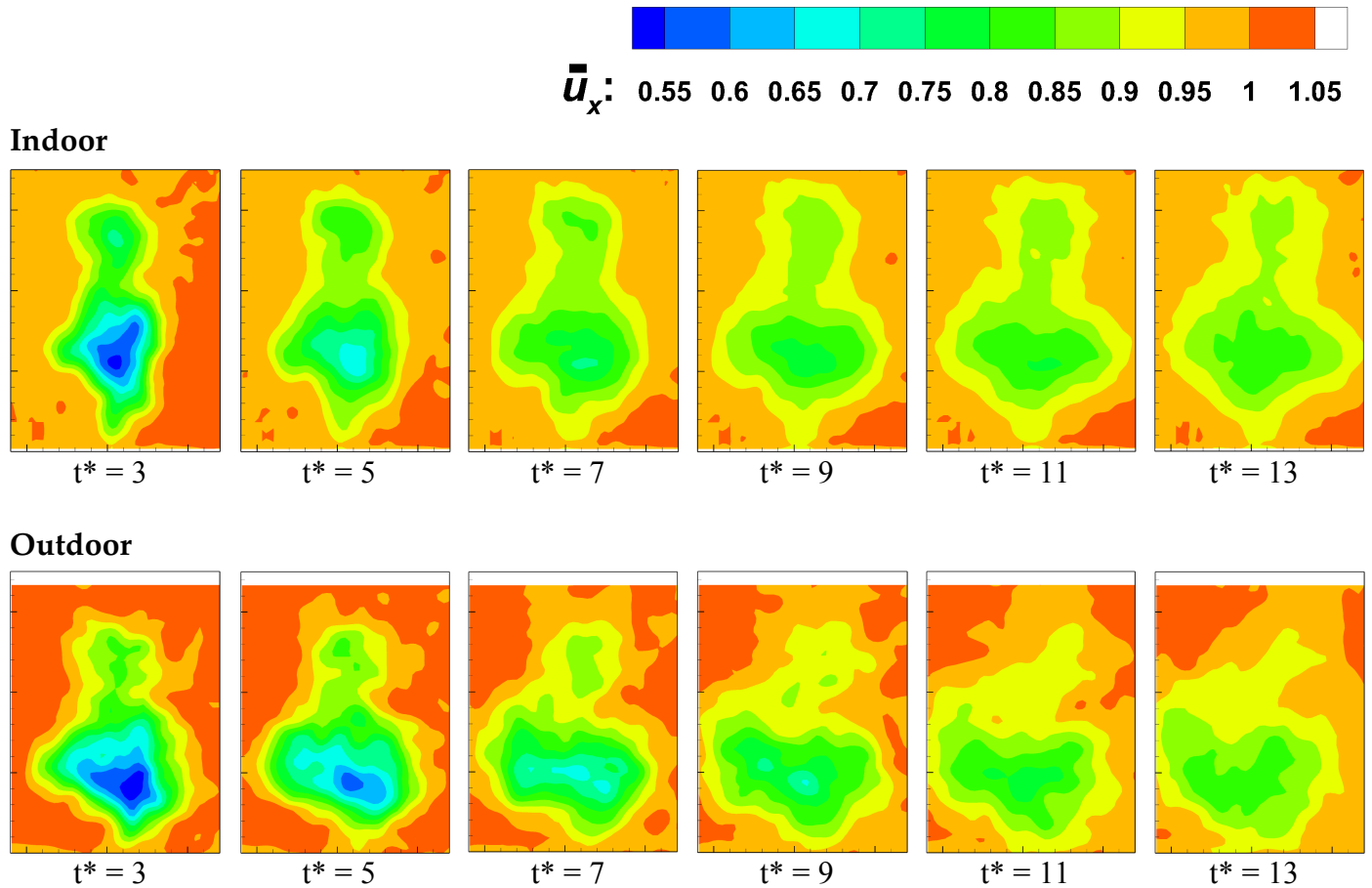


Fig. 9 Development of the dimensionless streamwise velocity deficit u_x over time. **Top:** indoor experiment. **Bottom:** outdoor experiment.

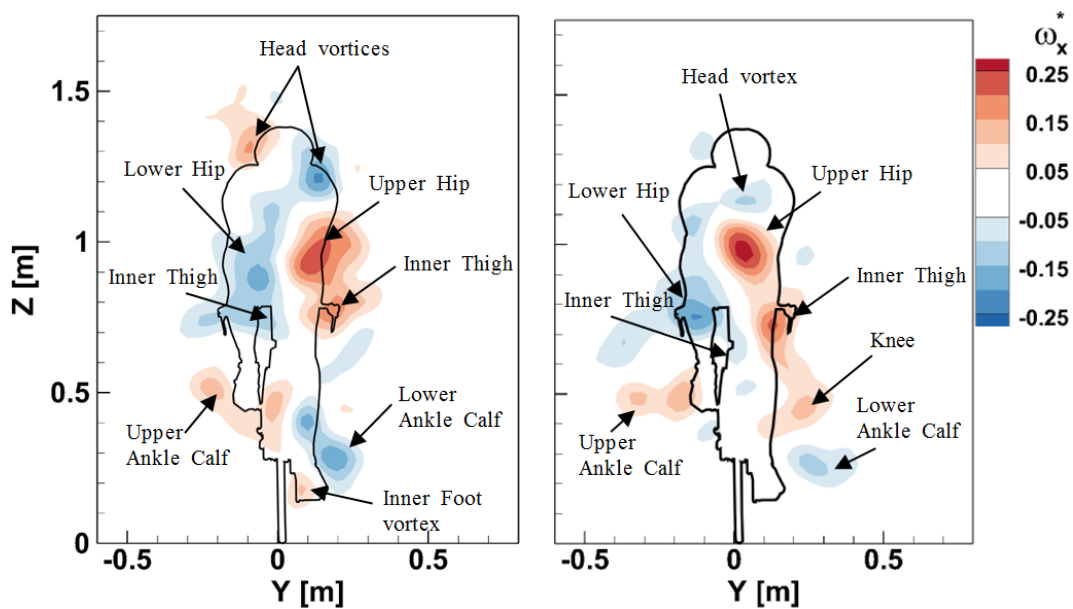


Fig. 10 Dimensionless streamwise vorticity ω_x^* at $t^* = 1.5$. **Left:** Indoor experiment; **Right:** Outdoor experiment.

4.2 Drag Analysis

4.2.1 Comparison of Dynamic Cases

Based on Equation 3 and on the procedures described in section 3.3, the instantaneous drag area $C_d A$ is computed for each test passage as a function of the dimensionless time t^* . In Fig. 11 five instantaneous test passages are shown for both the experiments with the cyclist pedalling in upright posture. In the outdoor experiment half a crank cycle is spanned along $\Delta t^* \approx 4$, while $\Delta t^* \approx 7.5$ for the indoor experiment.

In general it is noticeable that the drag area exhibits a steep growth in the near wake for $t^* \leq 3$ and then a plateau in the far wake. For the larger dimensionless times, instantaneous passages can show a sudden drop in the drag area, due to the motion of the wake out of the field of view. This is particularly evident in the outdoor experiment, in which the combination of external atmospheric conditions and a narrower field of view emphasizes the problem. When comparing the two experiments, it is noticeable that the outdoor experiment is affected by larger fluctuations, especially in the near wake. Differences among the instantaneous runs can be ascribed to variations in cyclist posture, unsteady fluctuations in the wake flow fields and measurement error.

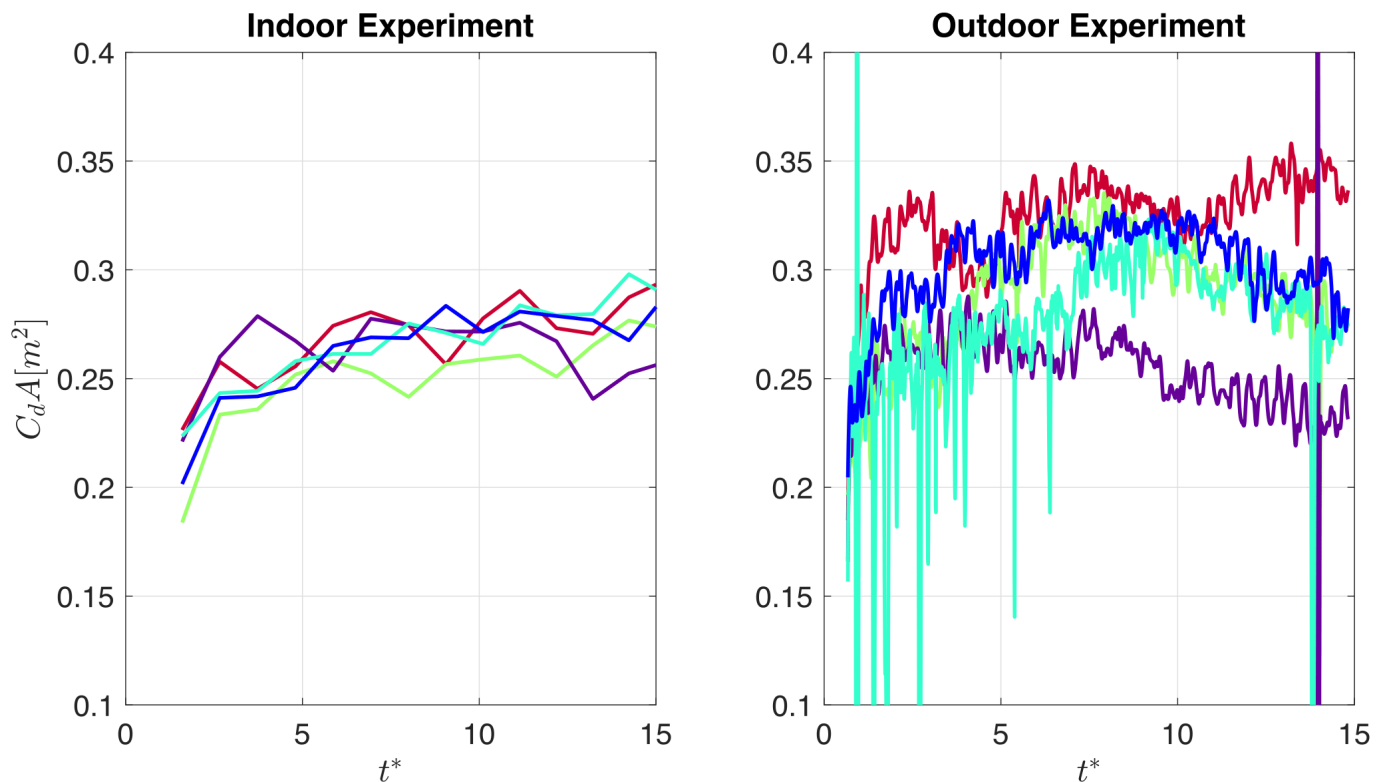


Fig. 11 Instantaneous Drag Area measurements with the cyclist in upright posture

In Fig. 12, the instantaneous drag areas are ensemble-averaged for both the time-trial and the upright postures. Together with the mean $C_d A(t^*)$, a shaded band wide $2\sigma_{C_d A}$ is shown. The same trend with the dimensionless time is underlined: the lower drag area in the near wakes can be attributed to the evaluation of the sole momentum term in Equation 3, thus the configuration drag area cannot be retrieved from this region as the wake has not recovered ambient pressure yet. Despite a similar mean trend for the time-trial posture, the two experiments differ in the upright posture drag area. In fact, the upright posture drag area is 18% higher than the time-trial one in the indoor experiment, while about 30% in the outdoor one. Notice that the outward wake motion in the far wake causes both a drop in the mean drag area and a larger standard deviation.

Interestingly, although both the experiments were designed to obtain phase-locked average data, no clear cyclic trend depending on the crank angle is visible. This result differs from the findings of Crouch et al. (2014), who highlighted a 20% drag area variation with the crank angle, for a fixed t^* . This outcome shows that the wake diffusion and turbulent mixing is the main phenomenon affecting the streamwise wake trend.

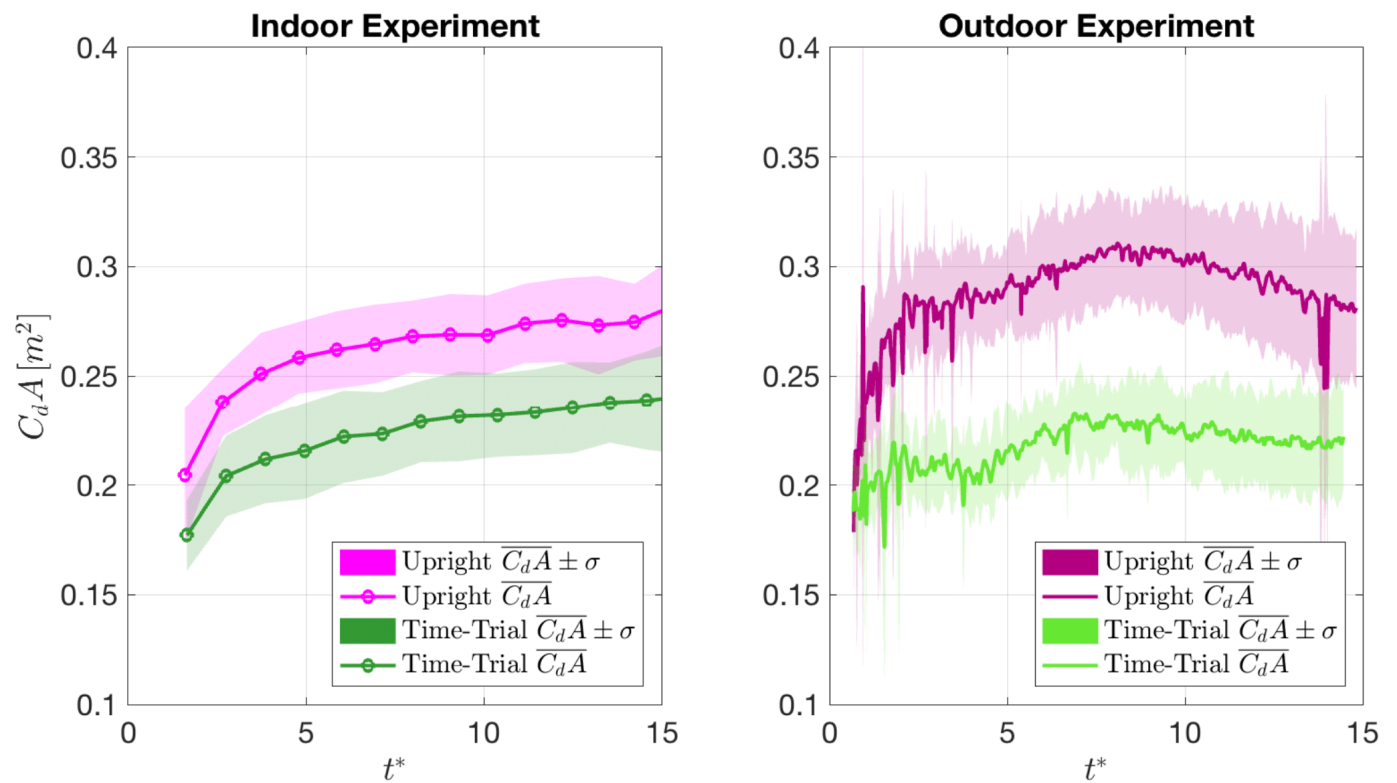


Fig. 12 Ensemble-averaged Drag Area measurements for Time-Trial and Upright postures

4.2.2 Comparison of Static Cases for the Indoor Experiment

In the comparison of the indoor experiment smaller drag area fluctuations were highlighted than in the outdoor experiment. This allows to distinguish smaller variations in the drag area between two postures as a time-trial asymmetric and symmetric configuration.

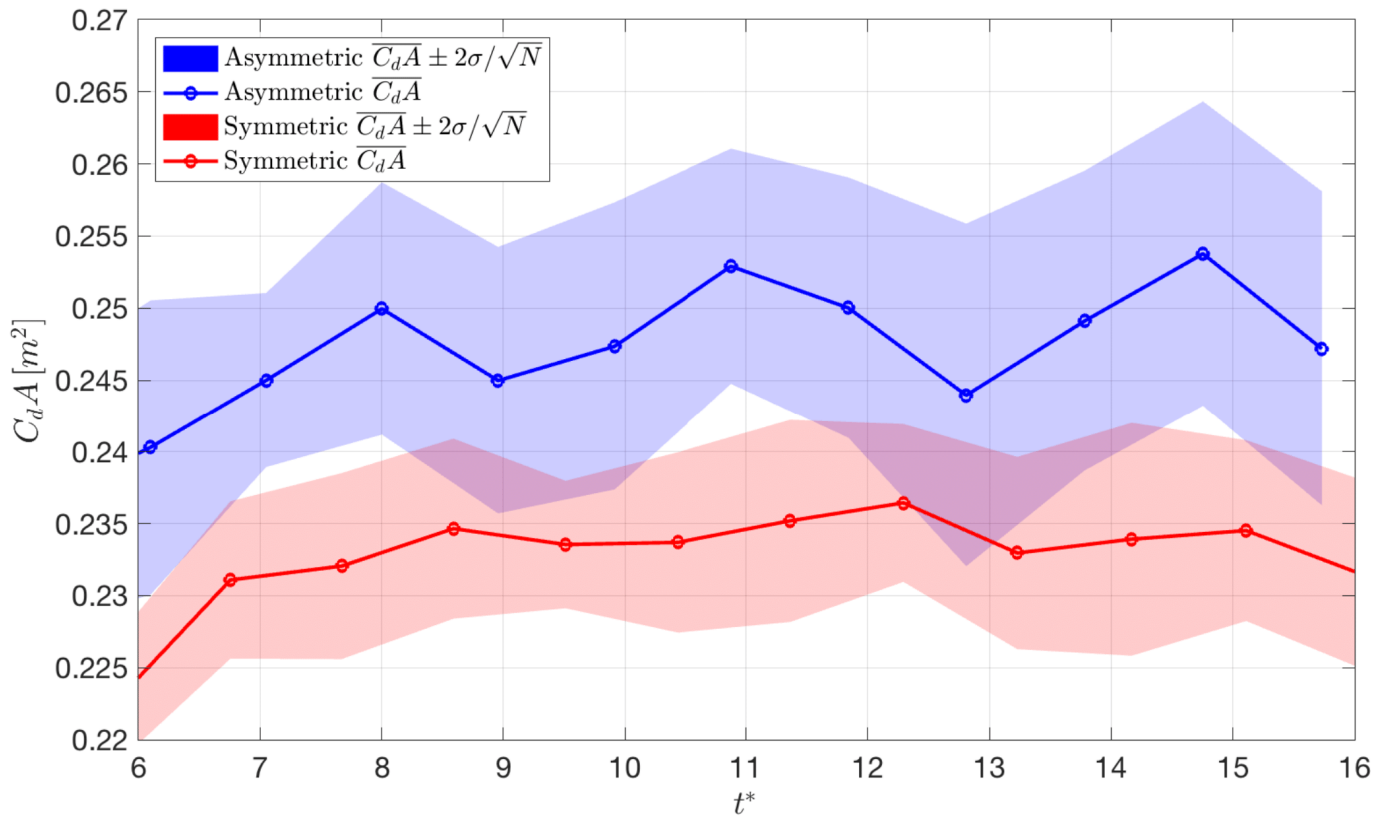


Fig. 13 Ensemble-averaged Drag Area measurements for Time-Trial Asymmetric and Symmetric leg postures

In Fig. 13 the results for the two static configurations are compared. The ensemble-averaged $C_dA(t^*)$ is plotted together with its uncertainty for a 95% confidence level. The asymmetric leg posture has a constantly higher drag area than the symmetric one, with a difference above 5%. During the experiment, the cyclist had difficulty in replicating the symmetric posture with the thighs aligned and in some cases the crank angle was above 15°. As a consequence, the symmetric posture drag area is over predicted on average, and this explains why a drag area difference about 20% (Crouch et al., 2014) is not found. Flow field analysis confirms this hypothesis as the symmetric posture does not show the a similar vorticity level for the quadrupole consisting of the two hip vortices and inner thighs vortices (Crouch et al., 2014, Griffith et al., 2014).

The experiment proves that the indoor Ring of Fire is suitable for detecting small drag differences ($\approx 5\%$) with less than twenty samples per case.

4.2.3 Overall Drag Area Summary

Finally, an overall drag area value is computed for each tested configuration. Because of the underpredicted drag area in the near wake and in the far wake, the overall configuration drag area is obtained by averaging across all the test runs and planes for $6 \leq t^* \leq 9$. Due to the high correlation among the streamwise wake planes, the uncertainty is computed over a restricted number of effective planes, evaluated following Sciacchitano and Wieneke (2016). The results are shown in Fig. 14.

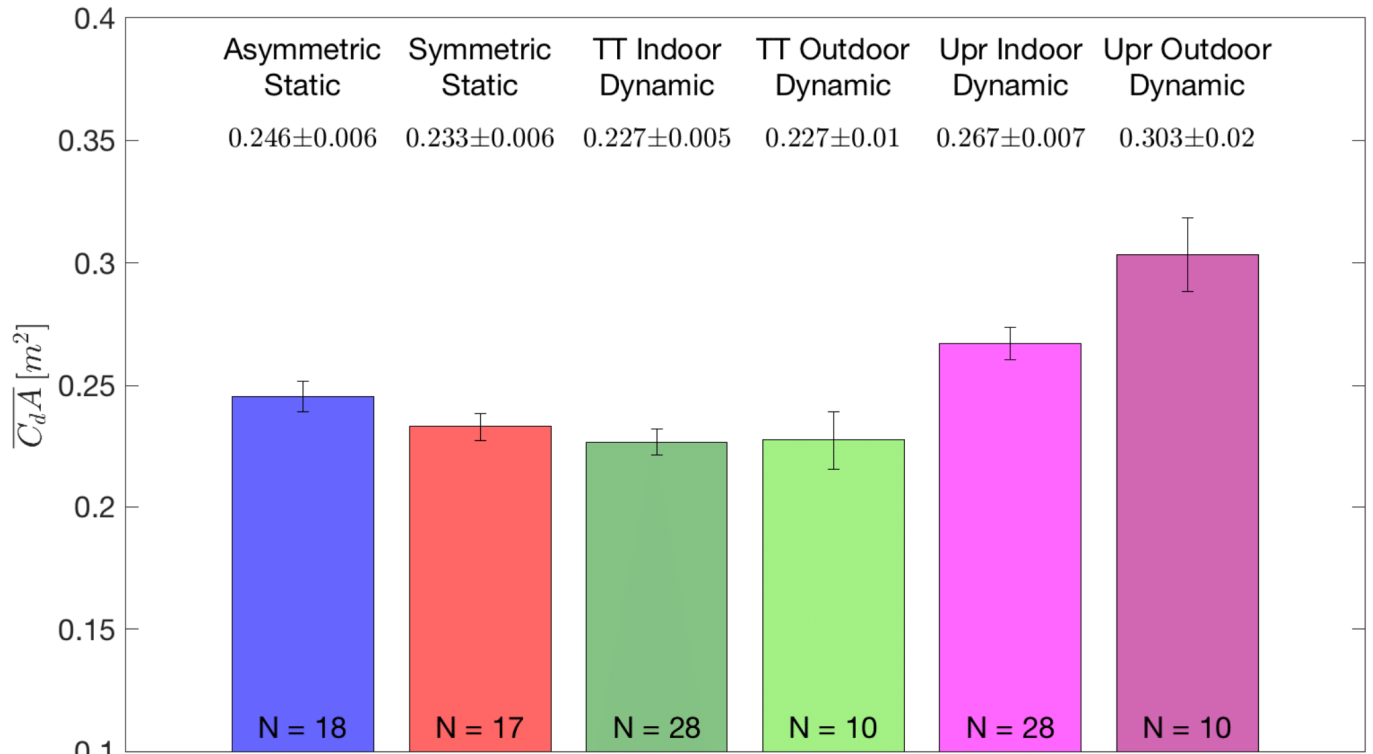


Fig. 14 Overall Drag Area summary; uncertainty bars for 95% confidence interval. N indicates the number of cyclist's passages per case

With less than twenty passages, the asymmetric and the symmetric leg postures can be unambiguously distinguished. Moreover, the mean dynamic time-trial drag area is the same in the two experiments. The indoor dynamic time-trial drag area is lower than the symmetric static drag area, as the latter is overestimated.

When static and dynamic cases are compared, the difference in uncertainty is solely due to the different amount of test passages. Therefore, this confirms once more that the fluctuations in drag area due to the pedalling cyclist do not affect the drag area standard deviation.

In addition, the two experiments show a difference in uncertainty mostly due to the difference in the number of test passages. In fact, if twenty-eight passages were used for the outdoor experiment uncertainty, it would be equal to $0.007m^2$ for the time-trial case and $0.009m^2$ for the upright one. The main difference between the two experiments is on the mean upright posture drag area: unfortunately there is no visual proof of the differences between the two postures and it can only be speculated that the different bike forced the rider to a lower torso angle in the indoor experiment.

In conclusion, an uncertainty on the mean of 2% can be obtained in the indoor experiment and 3% in the outdoor one, with about thirty passages and a confidence level of 95%. Moreover, the low-speed PIV system in the indoor experiment permits higher precision for $t^* \leq 6$.

5. Conclusions

Large-scale stereo-PIV measurements are conducted to determine the aerodynamic drag of a moving cyclist during indoor and outdoor on-site conditions using the control volume approach. The flow in the wake of a cyclist moving at 5 m/s and 8 m/s for respectively the indoor and outdoor conditions is measured. Instantaneous as well as ensemble-averaged streamwise velocity fields have been obtained and despite the fact that for both experiments the cyclist, the bike and the velocity was different, they compare well between both experiments and to literature. Furthermore, in the near-wake ensemble-averaged flow field, the wake structures that are observed are in both cases in good agreement to literature as well. The instantaneous and ensemble-averaged aerodynamic drag is evaluated via a control volume approach along the wake behind the cyclist. A clear distinction in upright vs. time-trial ensemble-averaged drag area is found for both experiments. The indoor experiment shows it is possible to distinguish smaller variations in the drag area between two postures, namely between a time-trial asymmetric and symmetric configuration. Small drag differences ($\approx 5\%$) with less than twenty samples per case are detected. A final remark that is worth mentioning is that the flow conditions prior to the passage of the cyclist, which is not equal in both experiments, need to be taken into account in the evaluation and may affect the measurement accuracy.

Acknowledgements

This research is supported by the Netherlands Organisation for Scientific Research (NWO) Domain Applied and Engineering Sciences (TTW), project 15583 “Enabling on-site sport aerodynamics with the ring of fire”

References

- Anderson J.D. (2011) *Fundamentals of Aerodynamics*. McGraw-Hill, New-York
- Blocken B, Defraeye T, Koninckx E, Carmeliet J, Hespel P. (2013) CFD simulations of the aerodynamic drag of two drafting cyclists. *Computers & Fluids*, 71:435-445.
- Bosbach J, Kühn M, Wagner C (2009) Large scale particle image velocimetry with helium filled soap bubbles. *Exp Fluids* 46:539–547
- Candau R, Grappe F, Ménard M, Barbier B, Millet G.Y., Hoffman M, Belli A, Rouillon J.D. (1999). Simplified deceleration method for assessment of resistive forces in cycling. *Medicine and science in sports and exercise*. 31(10):1441-7.
- Crouch, T., Burton, D., Brown N., Sheridan, J. , Thompson, M., (2016). Dynamic leg-motion and its effect on the aerodynamic performance of cyclists, *Journal of Fluids and Structures*, 65: 121-137.
- Crouch, T., Burton, D., Brown, N., Thompson, M., & Sheridan, J. (2014). Flow topology in the wake of a cyclist and its effect on aerodynamic drag. *Journal of Fluid Mechanics*, 748, 5-35.
- de Kat, R.; Bleischwitz, R. Towards instantaneous lift and drag from stereo-PIV wake measurements. In *Proceedings of the 18th International Symposium on the Application of Laser and Imaging Techniques to Fluid Mechanics*, Lisbon, Portugal, 4–7 July 2016.
- Defraeye T, Blocken B, Koninckx E, Hespel P, Carmeliet J. (2010) Aerodynamic study of different cyclist positions: CFD analysis and full-scale wind-tunnel tests. *Journal of Biomechanics*, 43:1262-1268.
- Gibertini G, Campanardi G, Guercilena L, Macchi C. (2010). *Cycling Aerodynamics: Wind Tunnel Testing versus Track Testing*. IFMBE Proceedings. 31: 10-13.
- Griffith M, Crouch T, Thompson M, Burton D, Sheridan J, Brown N. (2014). Computational Fluid Dynamics Study of the Effect of Leg Position on Cyclist Aerodynamic Drag. *Journal of Fluids Engineering*. 136.
- Jux, C., Sciacchitano, A., Schneiders, J.F.G., Scarano, F. (2018) Robotic volumetric PIV of a full-scale cyclist. *Exp Fluids* 59: 74.
- Keane, R.D. & Adrian, R.J. (1992) Theory of cross-correlation analysis of PIV images *Applied Scientific Research* 49: 191.
- Kyle C.R, Edmund, B (1984) Improving the racing bicycle. *Mechanical Engineering*. 106:34-35.
- Lukes R.A, Chin S.B, Haake, S. (2005). The understanding and development of cycling aerodynamics. *Sports Engineering*. 8:59-74.

Scarano, F., Ghaemi, S., Caridi, G.C.A. et al. (2015) On the use of helium-filled soap bubbles for large-scale tomographic PIV in wind tunnel experiments. *Exp Fluids* 56: 42.

Sciacchitano, A and Wieneke, B (2016) PIV uncertainty propagation *Meas. Sci. Technol.* 27 084006.

Sciacchitano, A., Scarano, F., Wieneke, B. (2012) Multi-frame pyramid correlation for time resolved PIV. *Exp Fluids* 53: 1087.

Shah, Y.H. Drag Analysis of Full Scale Cyclist Model Using Large-Scale 4D-PTV. Master's Thesis, TU Delft, Delft, The Netherlands, 2017.

Spoelstra, A.; Terra, W.; Sciacchitano, A. The Ring of Fire for in-Field Sport Aerodynamic Investigation. (2018). *Proceedings ISEA*, 2, 221.

Terra, W., Sciacchitano, A., & Scarano, F. (2016). Evaluation of aerodynamic drag of a full-scale cyclist model by large-scale tomographic-PIV. In *Proceedings of the International Workshop on Non-Intrusive Optical Flow Diagnostic: Delft, The Netherlands*

Wilson D.G. (2004) *Bicycling Science*. 3rd ed. MIT Press, USA.